Journal of Physics: Energy

PAPER

Towards low-cost sodium-ion batteries: electrode behavior of graphite electrodes obtained from spheroidization waste fractions and their structure-property relations

Ines Escher[1], **Marilena Mancini**[2], **Jan Martin**[2], **Knut Arne Janßen**[1], **Peter Axmann**[2] and **Philipp Adelhelm**[1,3,*]

[1] Humboldt Universität zu Berlin, Institut für Chemie, Brook-Taylor-Str. 2, 12489 Berlin, Germany
[2] Accumulators Materials Research (ECM) Zentrum für Sonnenenergie- und Wasserstoff-Forschung Baden-Württemberg (ZSW), Helmholtzstraße 8, 89081 Ulm, Germany
[3] Helmholtz-Zentrum Berlin, Joint Research Group Operando Battery Analysis, Hahn-Meitner-Platz 1, 14109 Berlin, Germany
* Author to whom any correspondence should be addressed.

E-mail: philipp.adelhelm@hu-berlin.de

Keywords: sodium-ion batteries, graphite, spheroidization, co-intercalation

Supplementary material for this article is available online

OPEN ACCESS

RECEIVED
2 August 2022

REVISED
24 November 2022

ACCEPTED FOR PUBLICATION
25 November 2022

PUBLISHED
19 December 2022

Abstract

Electrode materials for lithium-ion batteries (LIBs) typically show spherical particle shapes. For cathode materials, the spherical shape is obtained through the synthesis method. For graphite, the by far most popular anode material for LIBs, spherical particles are obtained through a spheroidization process. The yield of that process is quite low and limited to about 50%, leaving substantial amounts of by-products. Using such lower quality by-products would be quite attractive for developing low-cost energy stores like sodium-ion batteries (SIBs), for which the requirements for particle sizes and shapes might be less strict as compared to high performing LIBs. Here, we study three different graphite 'waste fractions' as anode material for SIBs that are obtained from the spheroidization process and how they compare to LIB battery grade material. Only negligible differences between the fractions are found when analyzing them with x-ray diffraction (XRD), Raman spectroscopy and elemental analysis (EA). More clear differences can be seen from N_2 physisorption, scanning electron microscopy (SEM) and particle size analysis. For example, the surface areas of the 'waste fractions' can become roughly up to twice as large as compared to the battery grade fraction and the d_{50} values shift by up to 11.9 μm to lower numbers. Electrochemical measurements show that the 'waste fractions' can deliver the full electrode capacity and behave similar to the battery grade fraction up to 10 C. However, the higher surface areas lead to more irreversible losses in the first cycle. A surprising finding is that all graphite fractions show almost identical discharge voltages, while the charging voltages differ by as much as 200 mV. This asymmetric behavior only occurs in SIBs and not in LIBs, which indicates a more complex storage behavior in case of sodium.

1. Introduction

The graphite used as anode material in lithium-ion batteries (LIBs) can be prepared synthetically from precursors or can be obtained from natural resources [1]. Both types consist of single-crystalline domains, which are oriented in the same direction in the case of natural graphite, whereas a more arbitrary orientation is present in the case of synthetic graphite [1]. In this manner, natural graphite particles tend to align with their basal plane (002 plane) parallel to the current collector [2, 3] and therefore result in a hindered diffusion (especially at high currents) of lithium ions as they are not able to enter between the graphene layers perpendicular to the basal plane [3–6]. To overcome this drawback, pristine natural graphite particles with flake morphology are generally spheroidized through a mechanical shaping process. Herein particles are

rendered into a more spherical shape-like form (potato shape) [5]. Typically, the shaping of the graphite particles leads to an increased tap density and easier processability during electrode manufacturing. Next to the particle shape, parameters such as particle size distribution and surface area are relevant too. The spheroidization process includes several steps in which undesired fractions (too large or too small particles) are removed.

Whereas the coarse fraction (overcorn) can be theoretically reused again in the spheroidization process [2] the fine fraction (smaller particles) can only be used in low-end applications, e.g. as lubricant or filling material [7]. Overall, the yield results in around 50% of the raw material [8]. The use of those 'waste fractions' for other battery chemistries with less strict requirements could therefore be quite appealing. One alternative to LIBs are sodium-ion batteries (SIBs) that are close in energy density but aim at using low-cost and less critical materials [9, 10]. It is important to note that graphite does not store larger amounts of sodium due to thermodynamic reasons [11, 12]. This would normally rule out its use as anode material for SIBs. However, graphite can be used in SIBs containing linear ethers as electrolyte solvents as these can co-intercalate into the graphite lattice along with the sodium ions rendering charge storage possible. Various aspects of this reaction have been addressed in the last years [13–43]. Just recently, graphite was combined with TiS_2 as co-intercalation cathode leading to a co-intercalation battery (CoIB) [44]. Formulas 1 and 2 show the conceptual difference between the conventional mechanism and the solvent co-intercalation mechanism for graphite. The intercalation of lithium ions into graphite follows the well-known multistage mechanism, with the lithium ions losing their solvation shell at the interface between liquid electrolyte and carbon material before being intercalated. Complete lithiation leads to a stoichiometry of LiC_6 ($n = 6$) which corresponds to a capacity of 372 mAh g^{-1} [45, 46]. The solvents of choice are mixtures of linear and cyclic carbonates, which decompose leading to the formation of a surface film (solid electrolyte interphase, SEI) that prevents any solvent co-intercalation [47, 48]. For sodium, intercalation is only possible through solvent co-intercalation which can occur for linear ethers (glymes) and few other solvents like ethylenediamine [34]. Values of 1–2 and 14–22 for y and n are typically found providing specific capacities between 100 and 162 mAh g^{-1}, mostly around 110 mAh g^{-1} [13, 15, 16, 19, 20, 22, 23, 26, 40].

$$C_n + e^- + Li^+ \rightleftharpoons Li^+C_n^- \tag{1}$$

$$C_n + e^- + Na^+ + y\,\mathrm{solv} \rightleftharpoons Na^+(\mathrm{solv})_yC_n^- \tag{2}$$

Few aspects of the solvent co-intercalation mechanism should be highlighted here. First, it leads to a large volume expansion of the electrode in every cycle [25, 29, 30, 34], pointing out the possible need of different graphite properties (e.g. particle size or porosity) for SIBs. Second, a major advantage of the co-intercalation reaction is the very good high C-rate behavior [15, 17, 24, 49], exceeding the already good performance of lithium intercalation in graphite [50, 51]. This might be related to the de-solvation step, which is not necessary in the case of sodium. Third, a major difference between these mechanisms is the formation of an SEI. Whereas it is commonly known for the lithium intercalation that an SEI is formed on the graphite surface in the first cycle, preventing a further electrolyte decomposition [52, 53], the existence of an SEI in the case of solvent co-intercalation is debatable [22, 25, 29, 33, 37, 41, 43]. Its existence very likely depends on the salt used [29, 37].

Commercial graphite is optimized to facilitate the intercalation of lithium ions in its structure. However, the insertion mechanism and properties are tremendously different compared to the sodium co-intercalation and the use of raw and only slightly purified graphite material with a carbon content of 55 wt% and 85 wt%, respectively (way lower compared to commercial graphite material) as host for sodium ions has already been shown by Laziz *et al* [38]. The low purity influences the specific capacity. However, a good cycling stability as well as the typical voltage profile can still be achieved [38].

In this work, several natural graphite fractions that are produced during a lab-scale spheroidization process [54] are physically characterized and their properties as negative electrode for SIBs are reported. The use of those 'waste fractions' would be another step towards more environmentally friendly batteries.

2. Methods

2.1. Spheroidization of graphite

The production process of the main fraction aimed for LIB-application (green fraction) is described elsewhere [54]. The fine (red) fraction that was separated from the green fraction during air classification was further separated into two fractions with the Picosplit 20 ATP classifier module of the Picoline

multiprocess mill (Hosokawa Alpine AG) using different process parameter. The obtained coarse fraction and fine fractions are named as orange and blue fraction, respectively.

2.2. Electrode preparation

The electrodes contained 90 wt% graphite and 10 wt% poly(vinylidene difluoride) (PVDF) (PI-KEM Ltd). *N*-methylpyrrolidone (NMP) was used as solvent during electrode production. The slurry was casted on a carbon coated Cu-foil (MTI-Corp.) and dried in air. The electrodes were punched out with a diameter of 12 mm and dried at 120 °C under vacuum overnight.

2.3. Electrochemical measurements

All electrochemical measurements were conducted in a two-electrode set-up using coin cells. 12 mm graphite electrodes were used as working electrode and 12 mm sodium (BASF) or lithium (Rockwood Lithium) discs as counter electrode. About 100 μl of 1 M NaOTf (purity > 98.0%, Sigma-Aldrich) in diglyme (2G, Sigma-Aldrich, pre-dried) and 1 M $LiPF_6$ in ethylene carbonate/dimethyl carbonate (EC/DMC, v/v, 1/1, Sigma-Aldrich) were used as electrolyte for the sodium and lithium cell, respectively. NaOTf was purified beforehand by dissolving in ethanol, reflux, hot filtration and drying for 24 h at 120 °C under vacuum. Two glass microfiber filters (GF/A) from Whatman with a diameter of 16 mm were used as separators.

All cycling experiments were conducted on a Biologic BCS 805. Galvanostatic charge and discharge with potential limitation (GCPL) experiments were conducted in a potential window of 0.01–2 V versus Na^+/Na or Li^+/Li with a C-rate of C/10 (11 mA g^{-1} for sodium and 37.2 mA g^{-1} for lithium). The mass loading of the active material varied from 4.7 to 5.8 mg cm^{-2} for the sodium cells and between 1.6 and 8.4 mg cm^{-2} for the lithium cells. Rate capability tests for the sodium cells were performed in the same voltage window and C-rates of C/3, 1 C, 5 C, 10 C, 20 C, 30 C, 40 C, 50 C, 60 C and again C/3 were applied. The mass loading of the active material varied from 4.8 to 7.5 mg cm^{-2}. Galvanostatic intermittent titration technique (GITT) were performed after two GCPL pre-cycles with a voltage window of 0.01 V–2 V versus Na^+/Na and a C-rate of C/10. For the GITT experiments the cells were (dis)charged for 30 min, followed by a 1.5 h waiting period. The lower and upper cut-off voltages during cycling were set to 0.01 V and 2 V versus Na^+/Na, the cut-off voltages after relaxation were set to 0.03 V and 1.9 V versus Na^+/Na. The mass loading of the active material varied from 5.9 to 7.9 mg cm^{-2}. Calculations of the diffusion coefficients are based on the following equation [55].

$$\tilde{D} = \frac{4}{\pi\tau}\left(\frac{m V_M}{M S}\right)^2\left(\frac{\Delta E_s}{\Delta E_t}\right)^2 \text{ valid for } \tau \ll L^2/\tilde{D}$$

where

π: the number Pi
τ: pulse length (s)
m: mass of the active material (g)
V_M: molar volume (V_m(graphite) = 5.29 cm^3 mol^{-1})
M_B: molar mass (M(carbon) = 12.01 g mol^{-1} (g mol^{-1})
S: geometrical surface area (1.13 cm^2) (m^2)
ΔE_S: change of the voltage during waiting time
ΔE_t: total transient voltage shift during the time when the current is applied
L: characteristic length (m)

To ensure steady state voltage, only data points were evaluated where the voltage shift did not exceed 5 mV h^{-1} within the last 5 min of the relaxation time.

We are aware that the boundary condition $\tau \ll \frac{L^2}{\tilde{D}}$ might not be fulfilled as the measured diffusion is very high which would require very small values for τ. Further limitations of the method must be mentioned. For reasons of simplification the geometric surface area (instead of the electrochemical active surface area) has been used and the square root time dependence of the transient voltage shift has shown partial deviation from ideal linear behavior.

2.4. Physical and chemical characterization

Scanning electron microscope (SEM) images were taken with a Phenom Pharos Desktop SEM from Phenom world using an accelerating voltage of 10 kV and a secondary electron detector.

X-ray diffraction (XRD) experiments were conducted with a D2 Phaser instrument from Bruker, using a Cu x-ray tube (30 kV, 10 mA). Experiments were performed between 5° and 80° using a step width of 0.05°.

Elemental analyses (EAs) were conducted on an Euro EA 3000 from EuroVector S.P.A. The provided values were the mean values of two measurements (red, orange and blue fraction) or three measurements (green fraction).

Brunauer–Emmet–Teller (BET) specific surface area evaluations have been conducted on adsorption isotherms measured with a 3Flex 3500 from Micromeritics Instrument Corp. at 77 K using nitrogen as adsorptive. The BET specific surface area was calculated in a relative pressure range p/p_0 between 0.04 and 0.3 using the Auto-Fit-Function of the measurement software.

Raman experiments were conducted using an inVia confocal Raman instrument from Renishaw with a laser wavelength of 532 nm. Data was acquired using five accumulations each having 20 s exposure time and a reduced laser intensity to 5%. Measurements were performed in the middle of the powder sample.

Particle size distribution measurements were done with a Mastersizer Micro MAF5000 from Malvern Panalytical.

3. Results and discussion

3.1. Physical characterization

Four different fractions of graphite particles have been investigated, including the fraction designed to be the target for LIBs. Figure 1 shows a schematic overview of the process starting from the raw material (natural graphite flakes). After spheroidization of the raw material and by using air-jet sieving and air classification, the green and red fractions are obtained. The green fraction represents the rounded product with target characteristics for LIBs, while the red fraction is the fine/'waste fraction' of the process. This remaining graphite fraction has been further split up into its course (orange) and fine (blue) fraction by a second air classification process.

SEM images (see figure 2) show that the spheroidization process for the green fraction was successful and round-shaped particles have been gained with a d_{50} particle size of 15.3 μm (see particle size distribution, figure 3). In contrast, the remaining fractions (red, orange and blue) consist of particles with platelet-like shape and d_{50} ranging from 3.4 μm (blue) over 4.9 μm (red) to 6.5 μm (orange). This is in line with the production route, designed to obtain the green fraction with the tailored particle size and the more spherical morphology.

Elemental analyses show that the carbon content is above 98% for every fraction, proving that only minor impurities are present. The amount of hydrogen shows a small increase with decreasing particle size, indicating a slightly higher defect content for the smaller particles. The amount of nitrogen and sulfur was in most of the measurements below the detection limit (see supporting information, table S1), evidencing the high purity of all samples.

Results from the surface analysis (specific surface area calculated with BET method from N_2 physisorption isotherms) are given in figure S1 (supporting information) and table 1. The BET specific surface area increases with decreasing the particle size, as expected, resulting in the lowest surface area for the green fraction (12 $m^2\ g^{-1}$) and the highest for the blue fraction (24 $m^2\ g^{-1}$).

Raman spectroscopy has been applied in order to study the properties of the graphite particles at the surface-near region. The ratio between the intensity of the D and G band reveals information about the amount of defects in the material. A typical example of measured Raman spectrum is shown in figure S2 for each sample. The samples were studied using different measurement settings and several locations of the samples were probed. Overall, no clear differences between the samples were found, indicating that the local structure of the different fractions is quite similar. This is further supported by XRD measurements, see figure S3. All samples are highly crystalline with defined peaks in the diffraction pattern. Asymmetric peaks (better visible on the (002) peak in figure S3(b)) indicate that different carbon phases/substructures exist in all different fractions [56]. However, no clear differences can be evidenced by XRD analysis between the different fractions, showing that the spheroidization process applied influences their crystal structure similarly.

Overall, the different fractions derived from the shaping process show very similar compositions (EA) and microstructures (XRD, Raman spectroscopy). As expected, the spheroidization leads to fractions with quite different particle sizes and, along with that, also slightly different specific surface areas. Key properties of all graphite materials are summarized in table 1.

3.2. Electrochemical investigation

Figure 4 represents the cycling performance of the four different graphite samples. Figure 4(a) shows that all graphite fractions, even the 'waste fractions', show a stable capacity of around 100–105 mAh g^{-1}. Common capacities gained in literature are in the range of 100–110 mAh g^{-1} [13, 16, 17, 19–22, 24, 25, 27, 29, 35, 41, 57], showing a sufficient intercalation of sodium ions into graphite for all fractions. This is close to the

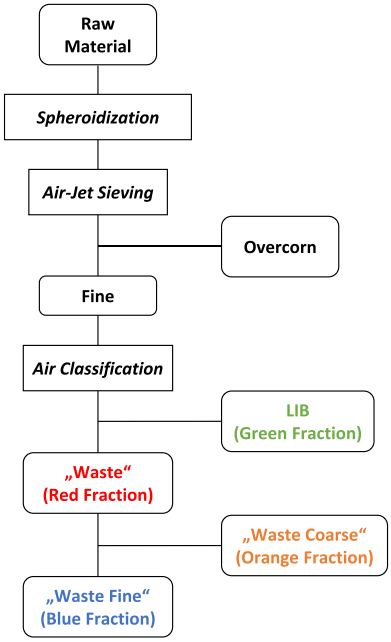

Figure 1. Overview of the production process of the different graphite fractions. The color code is used throughout the paper and indicates the 'target fraction' (battery graphite for LIB) as well as various 'waste fractions' with different particle sizes.

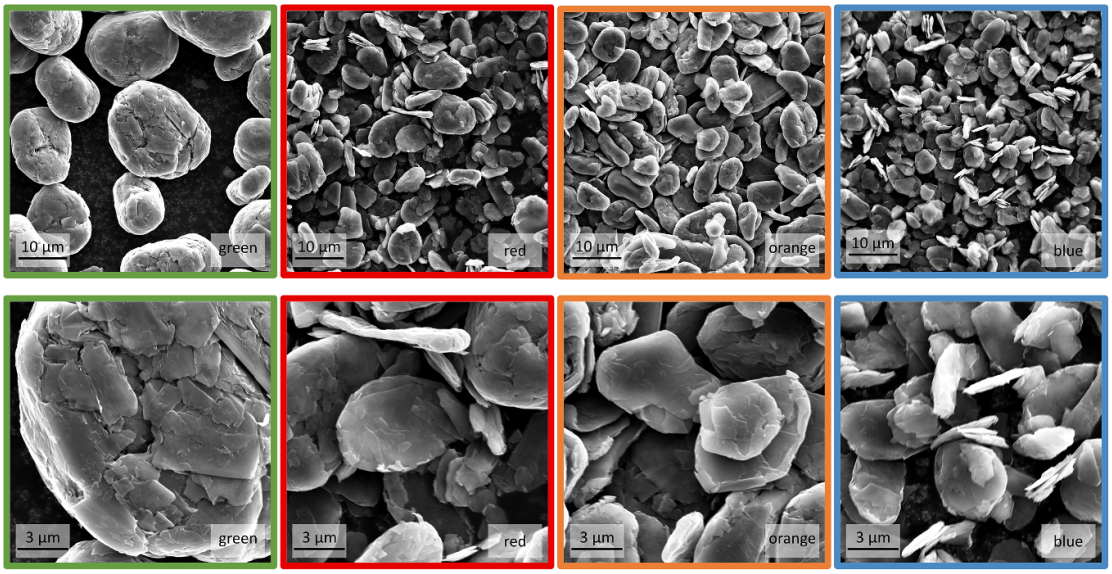

Figure 2. Scanning electron microscopy (SEM) images of the different graphite fractions.

theoretical capacity of 112 mAh g^{-1} for the formation of $Na^{+}(2G)_yC^{-}{}_{20}$, demonstrating that the particle size, shape or surface area do not influence significantly the ability to completely fill the graphite structure. This also proves the ruggedness of the co-intercalation reaction of sodium ions into graphite. However, it can be seen that different discharge capacities are obtained during the first cycle, reaching up to 206 mAh g^{-1} for the blue fraction. This is also displayed in figure 4(b) where a quite large irreversible capacity loss can be seen for the 'waste fractions' (red: 38%, orange: 39%, blue: 49%) compared to the LIBs 'target fraction' (green: 18%). The blue fraction, with the smallest particle size and the largest specific surface area, shows the highest irreversible capacity loss at the first cycle. In general, no or negligible SEI formation is assumed in the case of sodium-solvent co-intercalation in graphite with the salt used in this study [25, 29, 43]. However, due to the irreversible capacity losses observed, some side reactions may take place in this case at the electrode/electrolyte interface. These are related likely to the relatively high surface area (larger number of surface groups) of the carbon compared to the other fractions, and/or more pronounced side reactions with the binder. The latter effect might relate to a higher amount of binder being in contact with the electrolyte [41].

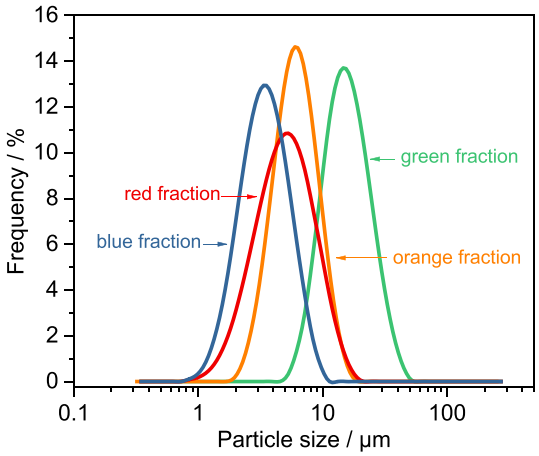

Figure 3. Volume based particle size distribution of the different graphite fractions derived from laser light scattering.

Table 1. Summary of the characteristics for the different graphite fractions.

Sample name	Particle size (d_{50}) (μm)	Morphology	Specific surface area (BET) ($m^2\ g^{-1}$)	Amount of carbon (EA) (wt%)	Amount of hydrogen (EA) (wt%)
Green	15.3	Round shaped	12	98.6	0.02
Red	4.9	Platelets	19	98.9	0.04
Orange	6.5	Platelets	17	98.9	0.04
Blue	3.4	Platelets	24	98.7	0.05

The origin of the irreversible capacity losses and its correlation with the surface area of the graphite used deserves deeper investigation and will be the subject of further studies.

In the following cycles (see figure 4(c) for the 100th cycle) the voltage curves are similar for the discharge process, leading to the expected voltage plateau at around 0.6 V and a sloping region afterwards [13, 15]. The typical voltage profile also confirms that a co-intercalation reaction is taking place for all graphite samples. However, the charging process for the different fractions shows some surprising differences according to the voltage profiles. No clear voltage plateau is visible for any of the different types of graphite, suggesting a slightly different de-intercalation process compared to the intercalation, as already proposed in literature [26]. This can be also seen from the derivative plots (dQ/dV) for which clear peaks are seen during sodiation and broad signals during de-sodiation, see figure S4. For the galvanostatic measurement, a more sloping behavior can be seen in following order: green < orange/red < blue, which is in line with a decreasing particle size and a higher BET specific surface area. In addition, the voltage gap between the charge and discharge processes increases in the same order. A similar behavior has been already observed and reported in literature for two different commercial graphite samples: the sample with higher surface area and lower crystallinity shows a more sloping charging profile and a higher overpotential, whereas no difference was visible in the discharge curves of the two graphite samples. However, no further explanation was given [13]. A linear correlation between the charge/discharge voltage gap, measured at the beginning of the 0.6 V plateau (corresponding to a specific capacity of 50 mAh g^{-1}, 100th cycle) and the BET surface value has been found, see supporting information figure S5. This suggests that the surface, and perhaps the ratio of surface to bulk of the particle has an influence on the voltage difference. While this is the only correlation we could identify, it also needs to be kept in mind that the particle morphology for the different fractions is not the same, see figure 2. It has to be pointed out that no differences can be seen in the voltage sloping region at lower potential values (0.6–0.01 V) between the four types of graphite for both discharge and charge. In this region, the graphite structure is already fully expanded and the storage mechanism appears more (pseudo)capacitive-like [25]. According to the systematic measurements shown here, this storage mechanism is identical for all samples, i.e. independent from the particle size and morphology.

GITT experiments were performed to identify more detailed differences between the samples and to study the degree of voltage relaxation. Figure 5(a) shows the comparison of the results obtained with the different samples. During discharge, the voltage values are all very close to each other, in good agreement

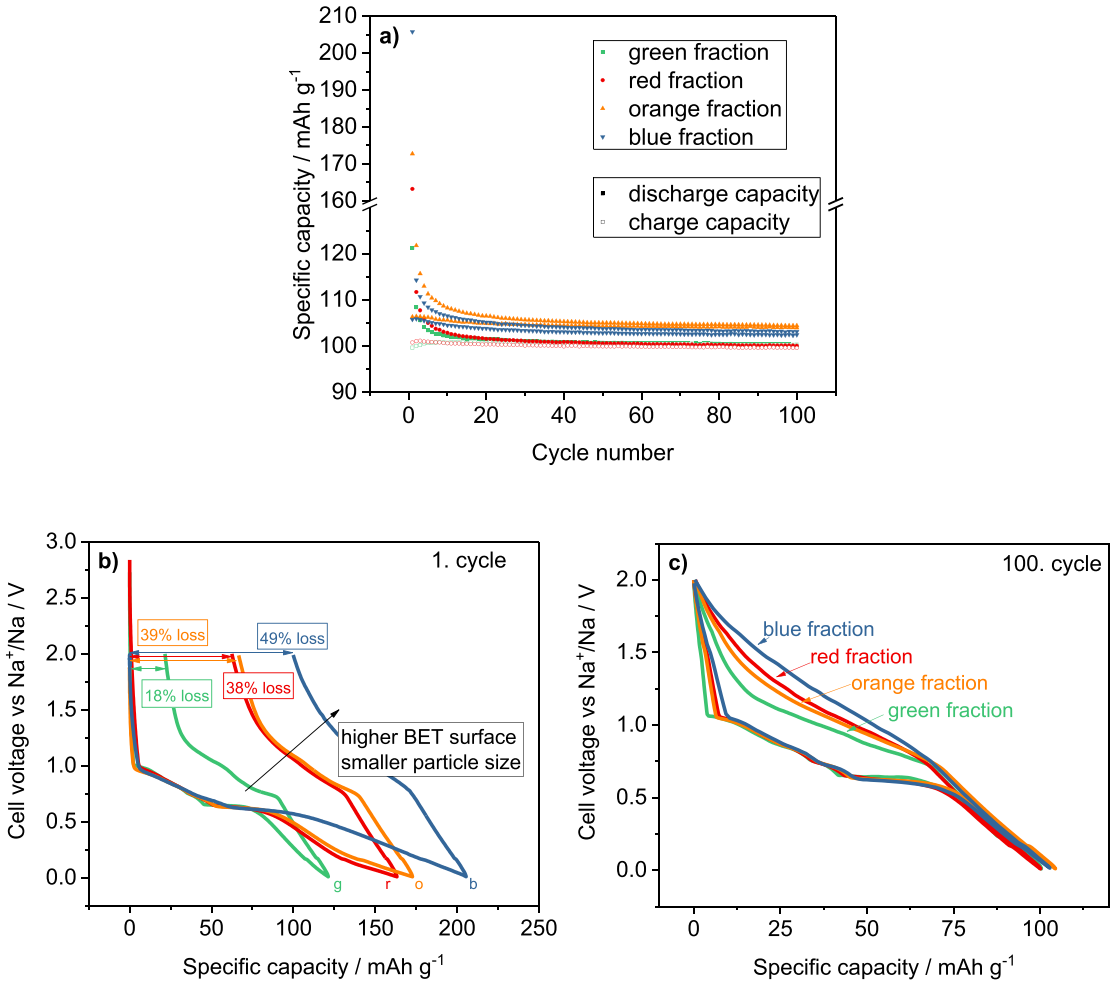

Figure 4. Galvanostatic cycling of sodium-ion cells with different graphite fractions as the working electrode and sodium as the counter electrode in a two-electrode set-up. Conducted with 11 mA g^{-1} using 1 M NaOTf in 2G as electrolyte. Different graphite fractions are abbreviated with their first letter. (a) Discharge and charge capacity over 100 cycles, (b) voltage profile of the first cycle and (c) voltage profile of the 100th cycle.

with galvanostatic measurement results. During charging, the differences are larger as can be better seen from the enlarged image in figure 5(b). For the green fraction (lowest voltage), the measured voltage decrease is 19.7 mV while for the blue fraction, the sample with the highest charging voltage, this value is 24.7 mV. The data indicate that the fraction with the highest surface area shows the largest polarization during charging, i.e. the asymmetric behavior might be a kinetic effect. On the other hand, the applied equilibration time does not lead to the same voltage value for all samples. Even after equilibration of over 1.5 h, there is still a difference of 12 mV between the green and the blue fraction. The small difference after relaxation might be due to instrumental limitations or the limited relaxation time of 1.5 h (even after several tens of hours no complete relaxation has been shown for other battery materials [58]). Despite those differences, the asymmetric behavior is quite evident. Currently we cannot fully explain this phenomenon. However, the results indicate that the solvent co-intercalation storage mechanism is a very complex involving processe that is so far not well understood. To further elucidate the diffusion processes in the different graphite fractions, the apparent (also called *effective*) diffusion coefficient D_{eff} is calculated out of the GITT data (see figures 5(c) and (d) with the equation given in the experimental part. The exact values have to be taken with precautions as the values for the surface area and the molar volume depend on the state of charge and are therefore not constant. A further discussion on the requirements is given in the experimental part. Two aspects appear relevant from the GITT measurements, which are in line with the findings from the galvanostatic measurements.

(a) D_{eff} is largest for the green fraction (largest particle size) and smallest for the blue fraction (smallest particle size). This is somewhat counter intuitive as one would expect an overall faster diffusion for

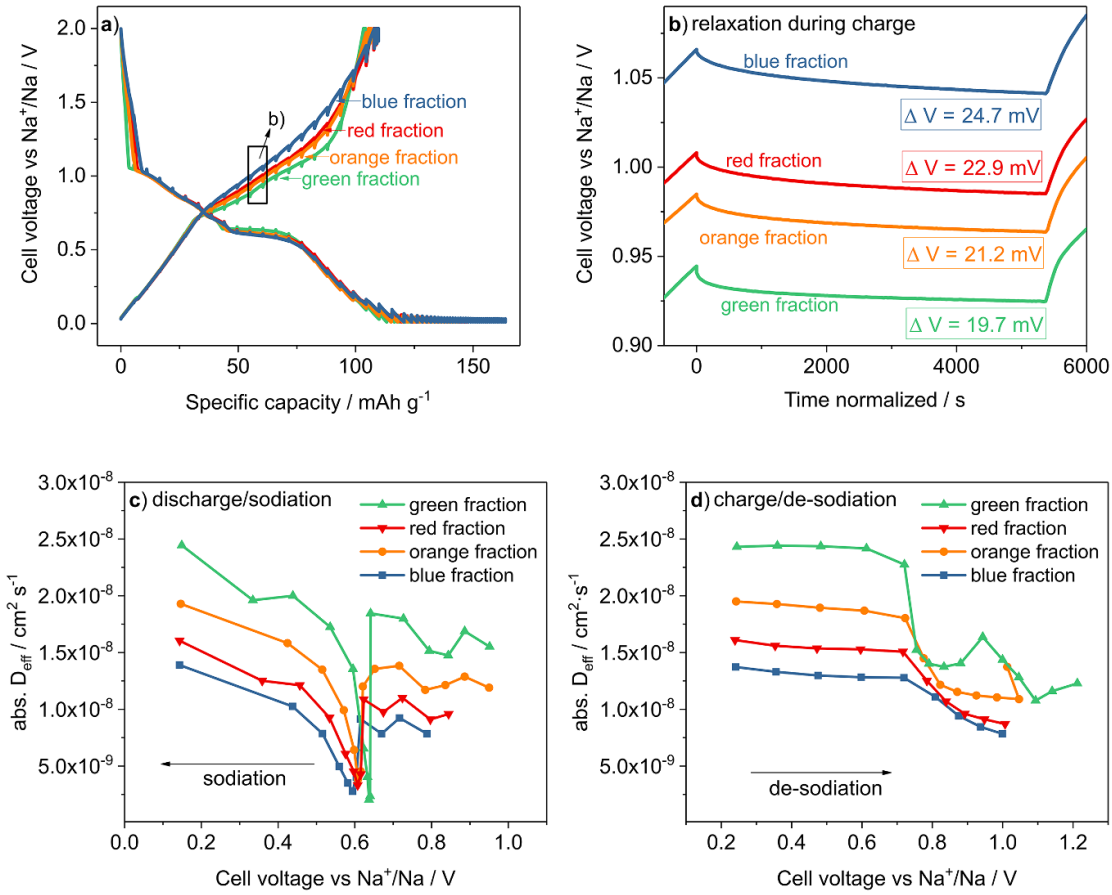

Figure 5. Galvanostatic intermittent titration technique (GITT) measurements of sodium-ion cells with different graphite fractions as the working electrode and sodium as the counter electrode in a two-electrode set-up. Conducted with 11 mA g^{-1} using 1 M NaOTf in 2G as electrolyte. (a) Voltage profile. The rectangle gives information about the part being enlarged in (b), (b) one relaxation step during charge with ΔV being the differences of the voltage before and after the relaxation time of 1.5 h, (c) apparent diffusion coefficient (D_{eff}) during discharge/sodiation, (d) apparent diffusion coefficient (D_{eff}) during charge/de-sodiation.

decreasing particle sizes. This is because the slowest process in many electrode reactions is the diffusion of ions in the crystal lattice. The diffusion of solvated ions in graphite is, however, very fast (even slightly faster than diffusion of lithium ions in graphite) [49]. This indicates that another factor is limiting the reaction kinetics. As the differences in electrode porosities (typically between 39% and 45%) and loadings (between 6 and 8 mg cm^{-2} for the GITT measurements) are relatively small, a possible cause might relate to the different particle morphologies, see SEM images in figure 2. Further information might be obtainable from *in situ* or *operando* studies such as dilatometry [59] or impedance spectroscopy which are sensitive to the dynamic behavior during cycling. These measurements, however, are outside the scope of the present study.

(b) Comparing the sodiation and de-sodiation process, it can be seen for all electrodes that the apparent diffusion coefficient sharply drops during co-intercalation/sodiation in the plateau region while a comparable behavior during de-intercalation/de-sodiation is not observed. This indicates further that the intercalation and the de-intercalation process differ from each other. Such an asymmetric behavior has been already observed during the co-intercalation of sodium and potassium ions in graphite [40, 60].

The asymmetric behavior between charging and discharging is not observed in case of lithium intercalation using a conventional standard electrolyte (1 M $LiPF_6$ in EC/DMC), see figure 6. In this case, the solvation shell is stripped during charge transfer and the naked lithium ions are intercalated to reach a graphite intercalation compound (GIC) with the final stoichiometry of LiC_6.

In lithium-ion cells, the 'waste fractions' show a higher irreversible capacity loss in the first cycle (red/orange: 22%, blue: 25%) compared to the green fraction (14%), which is expected due to the differences

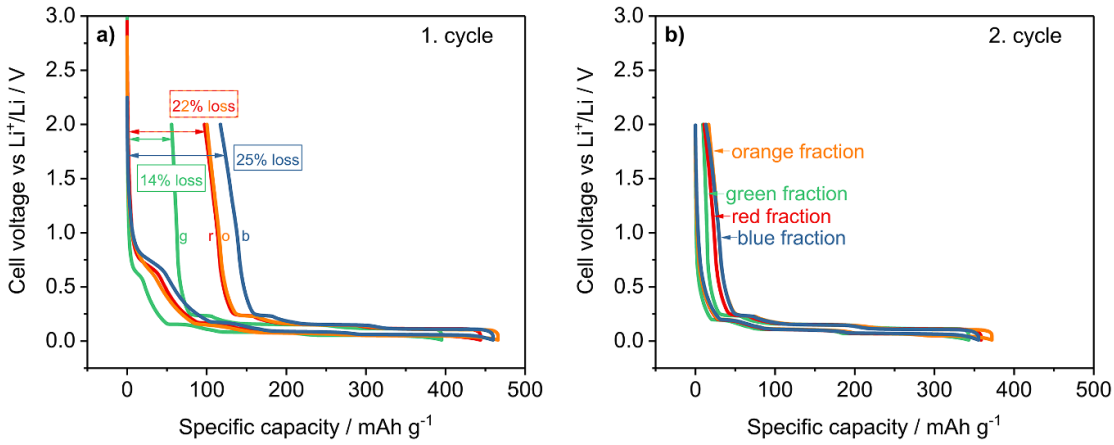

Figure 6. Galvanostatic cycling of lithium-ion cells with different graphite fractions as the working electrode and lithium as the counter electrode in a two-electrode set-up. Conducted with 37.2 mA g^{-1} using 1 M $LiPF_6$ in EC/DMC (v/v, 1/1) as electrolyte. Different graphite fractions are abbreviated with their first letter. (a) Voltage profile of the 1st cycle and (b) voltage profile of the 2nd cycle.

in specific surface areas and particle sizes. These results are in line with those obtained from sodium-solvent co-intercalation measurements. However, the voltage profiles for the lithium-ion cells show the expected behavior, i.e. they do not show the peculiar asymmetry between charge and discharge. No differences in overpotentials can be found for the different types of graphite during cycling, see figure 6(b) (2nd cycle). The voltage plateaus, indicating the staging mechanism during the intercalation of lithium ions [45], appear at very similar voltage values for all fractions during both charging and discharging. The asymmetric behavior described above (see figure 4) is therefore characteristic for the co-intercalation of sodium ions and solvent.

Figure 7 shows the results obtained from a symmetric rate test (sodium co-intercalation) for the different graphite fractions conducted at charging/discharging rates ranging between C/3 and 60 C. In agreement with the results discussed above, side reactions lead to a higher capacity in the first cycle, but values then quickly stabilize. During cycling at C/3 (~37 mA g^{-1}) values of around 105–110 mAh g^{-1} for all types of graphite (similar to cycling at C/10) are reached. Cycling at higher C-rates results to a slight drop in capacity, still resulting in 83–90 mAh g^{-1} at 10 C (1100 mA g^{-1}). The behavior is comparable for all graphite fractions up to a C-rate of 10 C. At higher current densities, the discharge capacity drops strongly for the green fraction, whereas higher values are obtained for the other graphite samples, especially for the blue and orange fraction. Cycling performance at very high C-rates strongly depend not only on the active material itself but also on other parameters at the electrode level, such as loading and porosity. Even though similar electrodes have been tested in this study for all graphite samples, deviations in these parameters do not allow conclusive data interpretation. Nevertheless, we can clearly observe that all fractions (not only the battery grade green fraction) show very good rate performance reaching 80% of their capacity (compared to the 5th cycle at C/3) at a C-rate of 10 C, which translates to discharging the cell in around 4.5–4.9 min. A generally good high C-rate behavior is visible in other studies on the co-intercalation of sodium ions in graphite as well [15, 17, 24, 35, 42]. Exceptionally high currents can be applied to some graphite material, enabling charge and discharge in 9 or 12 s [18, 35]. Voltage curves at different C-rates (see figures 7(b) and (c) reveal that, even though at low C-rates the main difference between the types of graphite is observed during the charging process, at high C-rates the voltage hysteresis is similar for all samples and the plateau at 0.6 V is not visible anymore due to polarization. In general, no significant differences can be seen between the different fractions in terms of high-rate performance in the sodium-ion cells. These results open the possibility of using 'waste graphite fractions', generated during the spheroidization process, in SIBs with high rate cycling performance. The results also suggest that, due to the different storage mechanism (and possibly different impact of the particle surface properties on the electrochemical behavior), the requirements—and thus the production cost—of graphite as active material in SIB applications are less demanding compared to the LIBs applications.

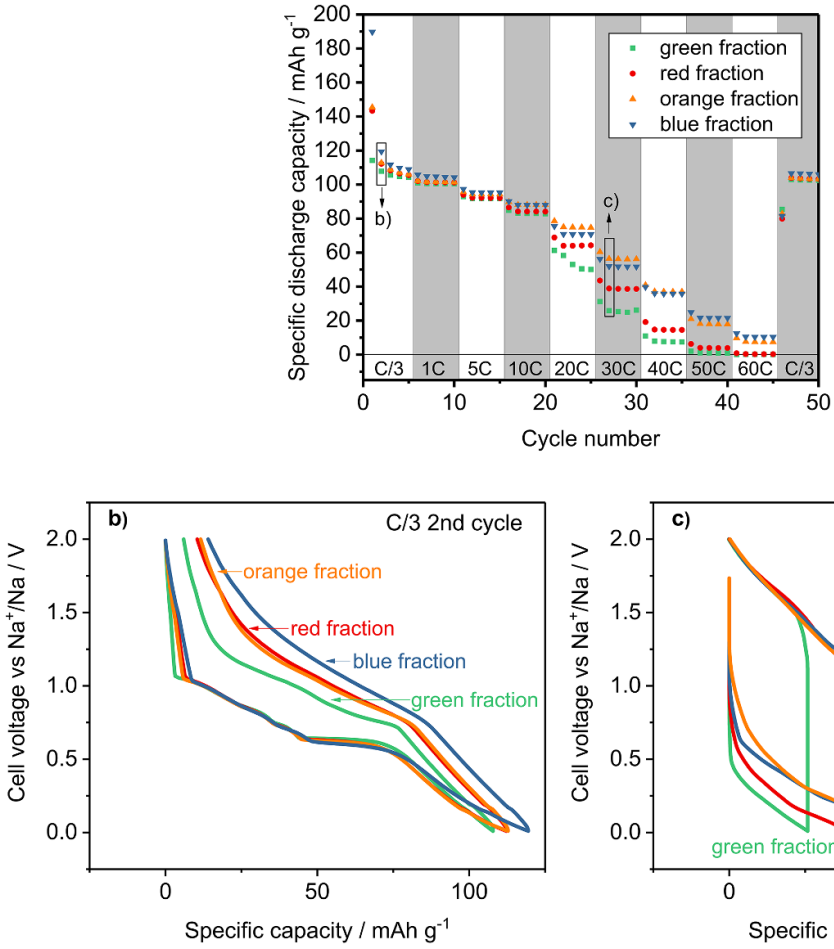

Figure 7. Rate capability test of sodium-ion cells with different graphite fractions as the working electrode and sodium as the counter electrode in a two-electrode set-up. 1 M NaOTf in 2G as electrolyte. (a) Overview of the specific discharge capacities for different C-rates (1 C corresponds to 110 mA g^{-1}), (b) voltage profile of the 2nd cycle with a C-rate of C/3, (c) voltage profile of the 2nd cycle with a C-rate of 30 C.

4. Conclusion and outlook

Four different graphite samples obtained from a lab-scale spheroidization process of natural graphite, were tested as anode material for SIBs. The process leads to a battery grade fraction (green) that is used for LIBs. The left-over 'waste fractions' (blue, red, orange) represent a potentially low-cost graphite source to be used for SIBs that aim a lower cost compared to LIBs. It was found that the fractions are quite similar with respect to their microstructure and composition but show, as expected, different particle size distributions and particle morphology. The particle sizes of the 'waste fractions' are smaller compared to the battery grade fraction and the morphology is more platelet-like. As expected, the smaller the particle size, the larger is the BET specific surface area. The larger values of BET specific surface area are likely a major cause for the lower initial Coulomb efficiencies of the 'waste fractions' when being used as anode in SIBs. However, the 'waste fractions' show stable cycling behavior at full capacity (~110 mAh g^{-1}) and exhibit good rate performance, e.g. 80% of the capacity is retained at a C-rate of 10 C. It can be concluded that those 'waste fractions' may be potential materials to be used in SIBs although the low initial Coulomb efficiency needs to be tackled before a practical use could be envisioned. Possible ways to overcome this problem would be surface modifications, the addition of electrolyte additives or a pre-cycling step. Even though the capacity gained is smaller for graphite compared to e.g. hard carbon it shows a very good high current behavior as well as a stable cycling and might find its application in this field.

A peculiar difference between the different fractions is found for the voltage profiles, which show an asymmetric behavior that is specific to the co-intercalation of sodium ions. While the discharge voltages are nearly identical for all fractions, clear differences up to about 200 mV are observed during charging. This

hints on a complex storage mechanism in case of sodium (with solvent co-intercalation) as this behavior is not observed for lithium ion intercalation in the same materials.

The present work demonstrates that by-product graphite produced during spheroidization can be successfully used as active material in SIBs and hence could be a potential low-cost source for their production.

Data availability statement

All data that support the findings of this study are included within the article (and any supplementary files).

Acknowledgments

The authors are grateful to Graphit Kropfmühl GmbH for providing the graphite raw materials. We also acknowledge the BMBF (Federal Ministry of Education and Research, Germany) for the funding project RONDO (03XP0112E). In addition, this project has received funding from the Deutsche Forschungsgemeinschaft (DFG, German Research Foundation, Grant Nos. 298787956 and 325774457), from the European Research Council (ERC) under the European Union's Horizon 2020 research and innovation programme (Grant Agreement No. 864698, SEED) and the EIG Concert Japan program (LIBRA, BMBF 01DR18003). The authors thank BASF for providing high purity sodium. We thank Ms. Markstein from the Humboldt Universität zu Berlin for the elemental analysis.

ORCID iD

Philipp Adelhelm https://orcid.org/0000-0003-2439-8802

References

[1] Asenbauer J, Eisenmann T, Kuenzel M, Kazzazi A, Chen Z and Bresser D 2020 The success story of graphite as a lithium-ion anode material—fundamentals, remaining challenges, and recent developments including silicon (oxide) composites *Sustain. Energy Fuel* **4** 5387–416
[2] Mundszinger M, Farsi S, Rapp M, Golla-Schindler U, Kaiser U and Wachtler M 2017 Morphology and texture of spheroidized natural and synthetic graphites *Carbon* **111** 764–73
[3] Yoshio M, Wang H, Fukuda K, Umeno T, Abe T and Ogumi Z 2004 Improvement of natural graphite as a lithium-ion battery anode material, from raw flake to carbon-coated sphere *J. Mater. Chem.* **14** 1754–8
[4] Ohzeki K, Saito Y, Golman B and Shinohara K 2005 Shape modification of graphite particles by rotational impact blending *Carbon* **43** 1673–9
[5] Ruggeri I, Martin J, Wohlfahrt-Mehrens M and Mancini M 2022 Interfacial kinetics and low-temperature behavior of spheroidized natural graphite particles as anode for Li-ion batteries *J. Solid State Electrochem.* **26** 73–83
[6] Wu Y-S, Yeh T-S, Lee Y-H and Lee Y-C 2011 Spheroidization modification of artificial graphite applied as anode materials for high rate lithium ion batteries *Adv. Mater. Res.* **201–203** 421–4
[7] Fu Y, Jin Y, Ma J, Liu J, Wang Z, Wang B and Gong X 2022 Lithium-ion transfer strengthened by graphite tailings and coking coal for high-rate performance anode *Chem. Eng. J.* **442** 136184
[8] Wu X, Yang X, Zhang F, Cai L, Zhang L and Wen Z 2017 Carbon-coated isotropic natural graphite spheres as anode material for lithium-ion batteries *Ceram. Int.* **43** 9458–64
[9] Vaalma C, Buchholz D, Weil M and Passerini S 2018 A cost and resource analysis of sodium-ion batteries *Nat. Rev. Mater.* **3** 18012
[10] Nayak P K, Yang L, Brehm W and Adelhelm P 2018 From lithium-ion to sodium-ion batteries: advantages, challenges, and surprises *Angew. Chem., Int. Ed. Engl.* **57** 102–20
[11] Liu Y, Merinov B V and Goddard III W A 2016 Origin of low sodium capacity in graphite and generally weak substrate binding of Na and Mg among alkali and alkaline earth metals *Proc. Natl Acad. Sci.* **113** 3735–9
[12] Lenchuk O, Adelhelm P and Mollenhauer D 2019 New insights into the origin of unstable sodium graphite intercalation compounds *Phys. Chem. Chem. Phys.* **21** 19378–90
[13] Jache B and Adelhelm P 2014 Use of graphite as a highly reversible electrode with superior cycle life for sodium-ion batteries by making use of co-intercalation phenomena *Angew. Chem., Int. Ed.* **53** 10169–73
[14] Han P, Han X, Yao J, Zhang L, Cao X, Huang C and Cui G 2015 High energy density sodium-ion capacitors through co-intercalation mechanism in diglyme-based electrolyte system *J. Power Sources* **297** 457–63
[15] Kim H, Hong J, Park Y-U, Kim J, Hwang I and Kang K 2015 Sodium storage behavior in natural graphite using ether-based electrolyte systems *Adv. Funct. Mater.* **25** 534–41
[16] Kim H, Hong J, Yoon G, Kim H, Park K-Y, Park M-S, Yoon W-S and Kang K 2015 Sodium intercalation chemistry in graphite *Energy Environ. Sci.* **8** 2963–9
[17] Zhu Z, Cheng F, Hu Z, Niu Z and Chen J 2015 Highly stable and ultrafast electrode reaction of graphite for sodium ion batteries *J. Power Sources* **293** 626–34
[18] Cohn A P, Share K, Carter R, Oakes L and Pint C L 2016 Ultrafast solvent-assisted sodium ion intercalation into highly crystalline few-layered graphene *Nano Lett.* **16** 543–8
[19] Hasa I, Dou X, Buchholz D, Shao-Horn Y, Hassoun J, Passerini S and Scrosati B 2016 A sodium-ion battery exploiting layered oxide cathode, graphite anode and glyme-based electrolyte *J. Power Sources* **310** 26–31

[20] Jache B, Binder J O, Abe T and Adelhelm P 2016 A comparative study on the impact of different glymes and their derivatives as electrolyte solvents for graphite co-intercalation electrodes in lithium-ion and sodium-ion batteries *Phys. Chem. Chem. Phys.* **18** 14299–316

[21] Kim H, Yoon G, Lim K and Kang K 2016 A comparative study of graphite electrodes using the co-intercalation phenomenon for rechargeable Li, Na and K batteries *Chem. Commun.* **52** 12618–21

[22] Seidl L, Bucher N, Chu E, Hartung S, Martens S, Schneider O and Stimming U 2017 Intercalation of solvated Na-ions into graphite *Energy Environ. Sci.* **10** 1631–42

[23] Yoon G, Kim H, Park I and Kang K 2017 Conditions for reversible Na intercalation in graphite: theoretical studies on the interplay among guest ions, solvent, and graphite host *Adv. Energy Mater.* **7** 1601519

[24] Goktas M, Akduman B, Huang P, Balducci A and Adelhelm P 2018 Temperature-induced activation of graphite co-intercalation reactions for glymes and crown ethers in sodium-ion batteries *J. Phys. Chem.* C **122** 26816–24

[25] Goktas M, Bolli C, Berg E J, Novák P, Pollok K, Langenhorst F, Roeder M V, Lenchuk O, Mollenhauer D and Adelhelm P 2018 Graphite as cointercalation electrode for sodium-ion batteries: electrode dynamics and the missing solid electrolyte interphase (SEI) *Adv. Energy Mater.* **8** 1702724

[26] Kajita T and Itoh T 2018 Mixed ether-based solvents provide a long cycle life with high rate capability to graphite anodes for Na-ion batteries *Phys. Chem. Chem. Phys.* **20** 2188–95

[27] Rodríguez-García J, Cameán I, Ramos A, Rodríguez E and García A B 2018 Graphitic carbon foams as anodes for sodium-ion batteries in glyme-based electrolytes *Electrochim. Acta* **270** 236–44

[28] Di Lecce D, Minnetti L, Polidoro D, Marangon V and Hassoun J 2019 Triglyme-based electrolyte for sodium-ion and sodium-sulfur batteries *Ionics* **25** 3129–41

[29] Goktas M, Bolli C, Buchheim J, Berg E J, Novák P, Bonilla F, Rojo T, Komaba S, Kubota K and Adelhelm P 2019 Stable and unstable diglyme-based electrolytes for batteries with sodium or graphite as electrode *ACS Appl. Mater. Interfaces* **11** 32844–55

[30] Karimi N, Varzi A and Passerini S 2019 A comprehensive insight into the volumetric response of graphite electrodes upon sodium co-intercalation in ether-based electrolytes *Electrochim. Acta* **304** 474–86

[31] Xu Z-L, Yoon G, Park K-Y, Park H, Tamwattana O, Kim S J, Seong W M and Kang K 2019 Tailoring sodium intercalation in graphite for high energy and power sodium ion batteries *Nat. Commun.* **10** 2598

[32] Divya M L, Natarajan S, Lee Y-S and Aravindan V 2020 Highly reversible Na-intercalation into graphite recovered from spent Li-ion batteries towards building high energy Na-ion capacitor with ultralong durability *ChemSusChem* **13** 5654–63

[33] Wang Z, Yang H, Liu Y, Bai Y, Chen G, Li Y, Wang X, Xu H, Wu C and Lu J 2020 Analysis of the stable interphase responsible for the excellent electrochemical performance of graphite electrodes in sodium-ion batteries *Small* **16** 2003268

[34] Escher I, Kravets Y, Ferrero A G, Goktas M and Adelhelm P 2021 Strategies for alleviating electrode expansion of graphite electrodes in sodium-ion batteries followed by *in situ* electrochemical dilatometry *Energy Technol.* **9** 2000880

[35] Wei Q, Chang X, Wang J, Huang T, Huang X, Yu J, Zheng H, Chen J-H and Peng D-L 2022 An ultrahigh-power mesocarbon microbeads|Na+-diglyme| $Na_3V_2(PO_4)_3$ sodium-ion battery *Adv. Mater.* **34** 2108304

[36] Patnaik S G, Escher I, Ferrero A G and Adelhelm P 2022 Electrochemical study of Prussian white cathodes with glymes-pathway to graphite-based sodium-ion battery full cells *Batteries Supercaps* **5** e202200043

[37] Maibach J, Jeschull F, Brandell D, Edström K and Valvo M 2017 Surface layer evolution on graphite during electrochemical sodium-tetraglyme co-intercalation *ACS Appl. Mater. Interfaces* **9** 12373–81

[38] Laziz N A, Abou-Rjeily J, Darwiche A, Toufaily J, Outzourhit A, Ghamouss F and Sougrati M T 2018 Li-and Na-ion storage performance of natural graphite via simple flotation process *J. Electrochem. Sci. Technol.* **9** 320–9

[39] Leifer N, Greenstein M F, Mor A, Aurbach D and Goobes G 2018 NMR-detected dynamics of sodium co-intercalation with diglyme solvent molecules in graphite anodes linked to prolonged cycling *J. Phys. Chem.* C **122** 21172–84

[40] Liang H-J, Hou B-H, Li W-H, Ning Q-L, Yang X, Gu Z-Y, Nie X-J, Wang G and Wu X-L 2019 Staging Na/K-ion de-/intercalation of graphite retrieved from spent Li-ion batteries: in operando x-ray diffraction studies and an advanced anode material for Na/K-ion batteries *Energy Environ. Sci.* **12** 3575–84

[41] Liu M, Xing L, Xu K, Zhou H, Lan J, Wang C and Li W 2020 Deciphering the paradox between the co-intercalation of sodium-solvent into graphite and its irreversible capacity *Energy Storage Mater.* **26** 32–39

[42] Jiang N, Hu Y, Bi W, Jiang H and Li C 2021 New insights on ultrafast Na[solv]+ coinserted graphite driven by an electric field *Sci. China. Mater.* **64** 2967–75

[43] Zhang X-R, Yang J-Y, Ren Z-Y, Xie K-Y, Ye Q, Xu F and Liu X-R 2022 *In situ* observation of electrolyte-dependent interfacial evolution of graphite anode in sodium-ion batteries via atomic force microscopy *New Carbon Mater.* **37** 371–9

[44] Alvarez Ferrero G, Åvall G, Mazzio K A, Son Y, Janßen K, Risse S and Adelhelm P 2022 Co-intercalation batteries (CoIBs): role of TiS 2 as electrode for storing solvated Na ions *Adv. Energy Mater.* 2202377 (https://doi.org/10.1002/aenm.202202377)

[45] Yoshio M, Brodd R J and Kozawa A (eds) 2009 *Lithium-Ion Batteries Science and Technologies* 1st edn (New York: Springer) (https://doi.org/10.1007/978-0-387-34445-4)

[46] Korthauer R (ed) 2013 *Handbuch Lithium-Ionen-Batterien* 1st edn (Berlin: Springer) (https://doi.org/10.1007/978-3-642-30653-2)

[47] Winter M 2009 The solid electrolyte interphase–the most important and the least understood solid electrolyte in rechargeable Li batteries *Z. Phys. Chem.* **223** 1395–406

[48] Xu K 2014 Electrolytes and interphases in Li-ion batteries and beyond *Chem. Rev.* **114** 11503–618

[49] Jung S C, Kang Y-J and Han Y-K 2017 Origin of excellent rate and cycle performance of Na+-solvent cointercalated graphite vs. poor performance of Li+-solvent case *Nano Energy* **34** 456–62

[50] Sivakkumar S R, Nerkar J Y and Pandolfo A G 2010 Rate capability of graphite materials as negative electrodes in lithium-ion capacitors *Electrochim. Acta* **55** 3330–5

[51] Buqa H, Goers D, Holzapfel M, Spahr M E and Novák P 2005 High rate capability of graphite negative electrodes for lithium-ion batteries *J. Electrochem. Soc.* **152** A474

[52] An S J, Li J, Daniel C, Mohanty D, Nagpure S and Wood III D L 2016 The state of understanding of the lithium-ion-battery graphite solid electrolyte interphase (SEI) and its relationship to formation cycling *Carbon* **105** 52–76

[53] Heiskanen S K, Kim J and Lucht B L 2019 Generation and evolution of the solid electrolyte interphase of lithium-ion batteries *Joule* **3** 2322–33

[54] Mancini M, Martin J, Ruggeri I, Drewett N, Axmann P and Wohlfahrt-Mehrens M 2022 Enabling fast-charging lithium-ion battery anodes: influence of spheroidization on natural graphite *Batteries Supercaps* **5** e202200109

[55] Weppner W and Huggins R A 1977 Determination of the kinetic parameters of mixed-conducting electrodes and application to the system Li_3Sb *J. Electrochem. Soc.* **124** 1569

[56] Popova A N 2017 Crystallographic analysis of graphite by x-ray diffraction *Coke Chem.* **60** 361–5
[57] Subramanyan K, Akshay M, Lee Y S and Aravindan V 2022 Na-ion battery with graphite anode and $Na_3V_2(PO_4)_3$ cathode via solvent-co-intercalation process *Adv. Mater. Technol.* 2200399
[58] Li B *et al* 2021 Correlating ligand-to-metal charge transfer with voltage hysteresis in a Li-rich rock-salt compound exhibiting anionic redox *Nat. Chem.* **13** 1070–80
[59] Escher I, Hahn M, Ferrero A G and Adelhelm P 2022 A practical guide for using electrochemical dilatometry as operando tool in battery and supercapacitor research *Energy Technol.* **10** 2101120
[60] Li L, Liu L, Hu Z, Lu Y, Liu Q, Jin S, Zhang Q, Zhao S and Chou S-L 2020 Understanding high-rate K+-solvent co-intercalation in natural graphite for potassium-ion batteries *Angew. Chem., Int. Ed. Engl.* **59** 12917–24